

Research Article

Direct Production of a Novel Iron-Based Nanocomposite from the Laser Pyrolysis of Fe(CO)₅/MMA Mixtures: Structural and Sensing Properties

R. Alexandrescu,¹ I. Morjan,¹ A. Tomescu,² C. E. Simion,² M. Scarisoreanu,¹ R. Birjega,¹ C. Fleaca,¹ L. Gavrilă,¹ I. Soare,¹ F. Dumitrache,¹ and G. Prodan³

¹Laser Department—Laboratory for Laser Photochemistry, National Institute for Lasers, Plasma and Radiation Physics, P.O. Box MG-36, 077125 Bucharest, Romania

²Laboratory of Low Dimensional Systems—Group of Gas Sensors, National Institute of Materials Physics, P.O. Box MG-7, 077125 Bucharest-Magurele, Romania

³Department of Chemistry, Ovidius University of Constanta, 900527 Constanta, Romania

Correspondence should be addressed to R. Alexandrescu, ralexandrescu2001@yahoo.co.uk

Received 30 October 2009; Accepted 8 January 2010

Academic Editor: Gong-Ru Lin

Copyright © 2010 R. Alexandrescu et al. This is an open access article distributed under the Creative Commons Attribution License, which permits unrestricted use, distribution, and reproduction in any medium, provided the original work is properly cited.

Iron/iron oxide-based nanocomposites were prepared by IR laser sensitized pyrolysis of Fe(CO)₅ and methyl methacrylate (MMA) mixtures. The morphology of nanopowder analyzed by TEM indicated that mainly core-shell structures were obtained. X-ray diffraction techniques evidence the cores as formed mainly by iron/iron oxide crystalline phases. A partially degraded (carbonized) polymeric matrix is suggested for the coverage of the metallic particles. The nanocomposite structure at the variation of the laser density and of the MMA flow was studied. The new materials prepared as thick films were tested for their potential for acting as gas sensors. The temporal variation of the electrical resistance in presence of NO₂, CO, and CO₂, in dry and humid air was recorded. Preliminary results show that the samples obtained at higher laser power density exhibit rather high sensitivity towards NO₂ detection and NO₂ selectivity relatively to CO and CO₂. An optimum working temperature of 200°C was found.

1. Introduction

The incorporation of nanoscale metal and metal-based particles into inorganic and polymeric/organic matrices represent an attractive field of research as compared to conventional phase-separated macrocomposites [1–3]. Due to the high-surface areas of the nanofillers and their molecular-level interactions with the matrix, there is great interest in nanocomposites due to significant scientific questions relating to interfacial chemistry and physics as well as their greatly enhanced practical properties. This is the reason why promising applications are expected in many areas: optics, electronics, ionics, mechanics, energy, environment, biology, medicine for example as membranes and separation devices, functional smart coatings, fuel and solar cells, and catalysts, sensor [4–6].

Methyl methacrylate (MMA) is a promising candidate for designing new nanostructured materials, as stabilizer and coverage component [7–9].

A large number of different semiconductor oxides have been investigated for their gas sensing properties. The sensing behavior of pure or doped Fe₂O₃ materials was studied for the optimization by nanoparticle processing [10, 11]. Addition of dopants decreases the film resistance and induces selectivity in sensor response [12].

The preparation of nanocomposite structures over thick film metal oxide gas sensors could provide advantages because they combine the properties of the inorganic fillers with the processability and flexibility of polymers and because they could be operated at lower temperatures [13, 14].

TABLE 1: Experimental parameters and EDAX analysis for the laser pyrolysis of MMA/Fe(CO)₅ mixtures. The pressure was maintained constant at 450 mbar.

| Samples | | | | | | P [W] | EDX at% | | | | |
|---------|--|--|---------------------------------------|--------------------------|---|-------|---------|-------|-------|------|------|
| | $\Phi_{\text{C}_2\text{H}_4}$ – MMA [sccm] | $\Phi_{\text{C}_2\text{H}_4}$ – Fe(CO) ₅ [sccm] | Φ_{Ar} – MMA [sccm] | Ar (add in) [sccm] | C ₂ H ₄ (add in) [sccm] | | C | Fe | O | Fe/C | Fe/O |
| MF03 | 10 | 60 | 0 | 60 | 0 | 50 | 26.04 | 44.63 | 29.33 | 1.71 | 1.67 |
| MF04 | 0 | 60 | 40 | 0 | 30 | 50 | 35.49 | 25.67 | 38.84 | 0.72 | 0.66 |
| MF06 | 0 | 60 | 30 | 0 | 30 | 50 | 32.74 | 28.32 | 38.94 | 0.86 | 0.72 |
| MF08 | 0 | 60 | 50 | 0 | 30 | 30 | 31.20 | 35.50 | 33.29 | 1.13 | 1.06 |
| MF09 | 0 | | 40 | 0 | 30 | 30 | 29.93 | 34.34 | 35.73 | 1.15 | 0.93 |
| MF10 | 0 | 60 | 40 | 0 | 30 | 70 | 35.21 | 21.97 | 42.82 | 0.62 | 0.51 |
| MF10h | | | Heated at 400 °C | | | | 31.24 | 21.49 | 47.27 | 0.69 | 0.45 |

We have reported recently on the formation of Fe/Fe₂O₃-based nano cores enveloped with polymeric polyoxocarbosilane shells [15]. The IR laser-induced pyrolysis from gas-phase reactants was used as synthesis technique [16]. A mixture containing iron pentacarbonyl (Fe(CO)₅) and hexamethyldisiloxane (HMDSO)—as iron and polymer precursors, respectively, and ethylene—as reaction sensitizer was employed. Thick films prepared from the low-polymer content Fe-based/polymer material were examined for the sensing capabilities, by testing the variation of the electrical resistance in presence of CO, and CH₄ gases, at a working temperature of 450°C [17].

In this paper, by applying the one-step laser pyrolysis to a gas mixtures containing Fe(CO)₅ and methyl methacrylate (MMA) we have prepared metal-based nanocomposites, presenting mainly core-shell structures. Different analytical techniques evidence the cores as formed mainly by iron/iron oxide crystalline phases. A partially degraded (carbonized) polymeric matrix is suggested for the coverage of the metallic particles. The nanocomposite structure at the variation of the laser density and of the MMA monomer flow was studied. Preliminary test on the sensing properties of the nanocomposite thick films were carried on by measuring the temporal variation of the electrical resistance in presence of NO₂, CO and CO₂, at a working temperature of 200°C. Rather high sensitivity towards NO₂ detection and selectivity to CO and CO₂ in the presence of water vapors was found for samples obtained at higher laser power density.

2. Experimental

Iron pentacarbonyl (about 28 mm Hg (4700 Pa) vapor pressure at 25°C) was employed as iron donor. MMA (C₅H₈O₂) was used as polymer precursor. The C₂H₄/Fe(CO)₅/MMA mixture was provided by bubbling C₂H₄ (which plays also the role of a sensitizer) or Ar through liquid Fe(CO)₅ and MMA, respectively, both held at ambient temperature (23°C). Argon flows of 1500 and 1100 standard cubic

centimetres per minute (sccm) were employed for gas confinement and cleaning the reactor windows, respectively. During the experiment, the pressure in the reactor is maintained constant (450 bar). Complementary ethylene or Ar flows were added either to help the reaction onset or to balance the flows, respectively. To avoid autoignition at the withdrawal in the atmosphere, the as-synthesized-nanoparticles were slowly in situ passivated.

The nanomaterials-labeled MF- were obtained at different laser power densities and different precursor flows. Table 1 shows the interrelated parameters for the different experimental conditions. Thus, the representative samples MF09, MF04, and MF10 are obtained for increased laser power densities of 30 W, 50 W, and 70 W, respectively. At the same laser power, the increase of MMA carrier flow from 30 sccm (MF06) to 40 sccm (MF04) and from 40 sccm (MF09) to 50 sccm (MF08) characterize the samples obtained at 50 W and 30 W, respectively.

The sensitive structures were obtained under the form of thick films by mixing the obtained Fe-based nanocomposite with an organic solvent and by depositing them on an alumina support equipped with Pt electrodes and heater. For performing sensing tests, the thick films were calcined at about 400°C (during 10 min) thus removing the organic solvent and improving the adherence onto the substrate. The last row of Table 1 refers to the properties of a representative calcined sample MF10h.

After synthesis, the morphology and composition of the nanocomposites were characterized by different analytical techniques: energy dispersive X-ray analysis (EDX) transmission electron microscopy (TEM), selected area electron diffraction (SAED), X-ray diffraction (XRD), and Infrared Spectroscopy (IR). The XRD patterns were collected on a PANalytical X'Pert MPD theta-theta system in continuous scan mode (counting 20s per 0.02 2 θ). In the diffracted beam, a Ni filter, a curved graphite monochromator and a programmable divergence slit, enabling constant sampling area irradiation, were placed ($\lambda = 0.15418$ nm). The samples were recorded under the very same conditions 45 KV and 40 mA.

The calcined nanocomposites (samples MFh: MFh03, MFh04, MFh08, and MFh10) were tested for the sensing capabilities using a DC-resistance measurement unit equipped with and electronically driven computer controlled Gas Mixing Station (Theoretic and Physic Institute, Tuebingen, Germany) [18]. The conductivity measurement facility allows for the determination of the electrical resistance R as a function of the temperature (the different temperatures of the active layers), the relative humidity (0–70% humidity) and the gas concentration. The resistance of the films has been monitored during the controlled exposure to NO_2 , CO , and CO_2 with test concentrations of 300–1000 ppb, 15–100 ppm and 700–4000 ppm, respectively. Different gas atmospheres were obtained by mixing synthetic air (5.0 purity) with nitrogen dioxide, carbon monoxide, and carbon dioxide (5.0 purity). The gas supply was carried out for 60 minutes for each gas according to the following listing: NO_2 (300, 500, 700, 1000 ppb), CO (15, 30, 70, 100 ppm), and CO_2 (700, 100, 3000, 4000 ppm). For each gas, the sensitivity tests were performed in dry and humid atmosphere (50% RH). Through the conductivity measurements 4 target temperatures (400, 350, 250, and 200°C) were fixed in order to test the sensors and were activated ranging from the highest to the lowest temperature. The reversibility of the sensor performance was evaluated by supplying synthetic air after each supply of test gas.

3. Results and Discussions

The laser decomposition of both MMA and iron pentacarbonyl is chiefly based on the excitation of ethylene (IR photosensitizer) and a collisional energy transfer between the excited ethylene and these compounds. The CO_2 laser decomposition of $\text{Fe}(\text{CO})_5$ results in the formation of elemental iron along with carbon monoxide. We should mention that a detailed description of MMA polymerization and consequent degradation routes is beyond the scope of this work. However, the analysis of our results allow for some phenomenological comments. It was shown [19] that in the laser homogeneous decomposition of methyl methacrylate dominant acyl-oxygen and C-Me cleavage reactions occur and generate radical-chain mechanism. On the other hand, by using a pulsed IR laser radiation, molecular elimination reactions with formation of gas-phase products such as methane, acetylene, CO_2 , and CO were observed [20]. Thus, accounting for in terms of polymerization of the transiently produced radicals, the polymerization of volatile MMA organic monomer into poly(methyl methacrylate) (PMMA), with variable cross-linking degree is suggested. At the same time, due to the reaction temperature in the IR laser pyrolysis (about 650°C) a partial degradation (carbonization) should occur (pure PMMA decomposition can start even at 150°C [21]). The possible formation of a PMMA as a polymeric matrix is suggested by the IR analysis of nanopowders (see below). On the other hand, the thermal initiation of MMA polymerization is confirmed by the literature [22] and is attributed to the presence of peroxide containing species that are formed from dissolved oxygen and the monomer itself.

These peroxides decompose quickly and initiate the radical polymerization. Another major aspect refers to the particular conditions of the sensitized pyrolysis, since the freshly formed iron nanoparticles (resulted from carbonyl dissociation) could play an important surface-catalytic role. The iron-mediated polymerization of MMA has been reported by studying the catalyzing effects of the temperature and fine particles of Fe_2O_3 upon methyl methacrylate (MMA) thermal polymerization (see [23]). Recently, ferrocene-based [24] and Ziegler-Natta type [25] catalyst systems were used to greatly improve MMA polymerization. The interaction of nanoscale iron and (un)degraded PMMA matrix was also confirmed by Mossbauer and IR spectra [26].

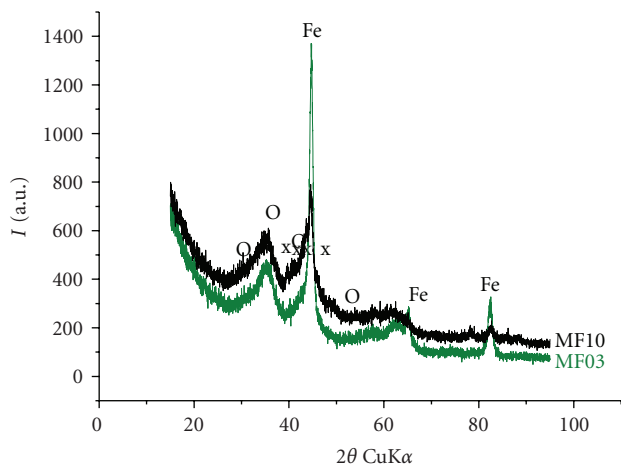
3.1. Energy Dispersive X-Ray (EDX) Analysis. The elemental content (in at %) of carbon, oxygen, and iron (averaged values for the measurements in three different points) found in the as-synthesized samples and in the MF10h heated one are presented in Table 1. EDX data Fe/C and Fe/O atomic ratios allow for a better comparison of the compositional evolution of samples with the varying experimental conditions (last two columns in Table 1). We should note that the oxygen presence could be explained either by the uptake at the withdrawal of the nanocomposite in the ambient or by transient oxygen-containing radicals appearing in MMA induced decomposition. From the EDX analysis one observes the rather high carbon content of all samples, entering in the composite matrix under different forms (turbostratic carbon and/or polymer fragments). The source of carbon could be both MMA and ethylene (unwanted) dissociation. It is worth to note that in this respect, EDX reveals special features for the sample MF03 obtained at very low ethylene flows and which exhibits lower carbon (26 at %) content. We should mention that a small part of this carbon could participate to the minor iron carbide phase formation, as evidenced by X-ray analysis (see below). It is worth to note the increased carbon quantity with increasing laser power (Fe/C decreases from 1.15 to 0.62 for samples MF09 (30 W) and MF10 (70 W), resp.).

3.2. XRD Analysis. The XRD spectra of all as-synthesized MF samples (Figures 1 and 2) show a mixture of two major crystalline phases: the magnetite-maghemite Fe_2O_3 oxide phase and the Fe-phase. The crystalline network constants for the crystalline phases and the crystallite dimensions are estimated in Table 2.

In Figure 1, the XRD patterns of samples MF10 and MF03 obtained at different reaction temperatures (high and low ethylene flows, resp.) are exposed. The spinel-type iron oxide phase is characterized by extremely broad peaks due to very small size crystallites associated to high structural disorder. The peak broadening prevents distinguishing between the magnetite- Fe_3O_4 and the maghemite- $\gamma\text{-Fe}_2\text{O}_3$ phases. Cementite Fe_3C phase appears as traces and is more pronounced (even as a minority phase) at higher reaction temperature (sample MF10.) This phase is missing in case of MF03. The inset in Figure 1 presents the dependence of

TABLE 2: Comparative XRD evaluation of some of the structural parameters of samples obtained from MMA/Fe(CO)₅ mixtures (network constants and Scherrer mean crystallite dimensions).

| Samples | Network constants | | | | | | | Crystallite dimensions (nm) | | | | Obs. |
|---------|-------------------|---|--|-------|-------|---|-------|-----------------------------|--|-------------------|---|--------------------------|
| | Fe a (Å) | γ -Fe ₂ O ₃ /Fe ₃ O ₄ a (Å) | Fe ₃ C a (Å) b (Å) c (Å) | | | α -Fe ₂ O ₃ a (Å) c (Å) | | Fe | γ -Fe ₂ O ₃ /Fe ₃ O ₄ | Fe ₃ C | α Fe ₂ O ₃ | |
| MF03 | 2.866 | 8.399 | — | — | — | — | — | 9.7 | 2.0 | — | — | |
| MF04 | 2.867 | 8.397 | — | — | — | — | — | 9.4 | 2.0 | — | — | Fe ₃ C traces |
| MF06 | 2.852 | 8.394 | — | — | — | — | — | 10.8 | 1.6 | — | — | Fe ₃ C traces |
| MF08 | — | 8.401 | — | — | — | — | — | — | 1.9 | — | — | |
| MF09 | — | 8.370 | — | — | — | — | — | 8.8 | 1.8 | — | — | |
| MF10 | 2.859 | 8.391 | 5.065 | 6.614 | 4.522 | — | — | 13.6 | 2.1 | 17.6 | — | Minor Fe ₃ C |
| MF10h | — | 8.35 | — | — | — | 5.02 | 13.71 | — | 12.4 | — | 31.5 | |



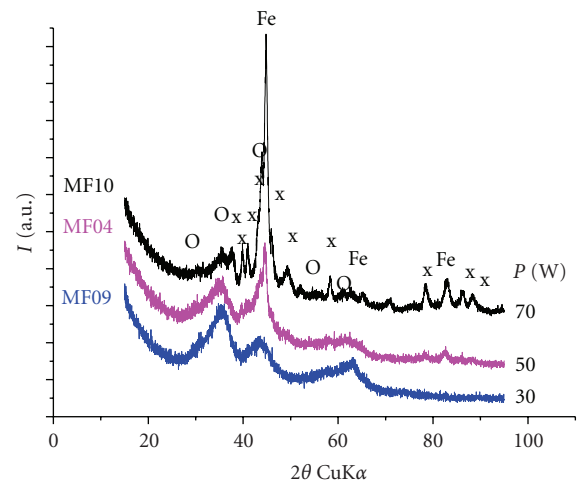
O: γ -Fe₂O₃-Fe₃O₄
x: Fe₃C

FIGURE 1: XRD patterns of samples obtained at different reaction temperatures: high ethylene flow (MF10) and low ethylene flow (MF03). The inset represents the dependence of the Fe₁₁₀ reflection (absolute maximum) on the Fe content (at %)—as determined from EDX measurements.

the Fe₁₁₀ reflection (absolute maximum) on the Fe content (at %) as determined from EDX measurements.

XRD patterns of samples obtained at three different laser powers: MF10 (70 W), MF04 (50 W), and MF09 (30 W) are presented in Figure 2. One may observe that the phase composition is highly sensitive to the laser power since important changes are induced. At low power (30 W-samples MF08, MFO9), the oxide phase (γ -Fe₂O₃/Fe₃O₄) prevails. At 50 W the Fe phase is straightened, the oxide phase remains and possible Fe₃C traces appear. The highest amount of the Fe phase and, besides the oxide phase, clearly emerging peaks of the Fe₃C phase are found in samples synthesized at 70 W [27].

Another remark regards the laser power effect on the amount of the oxide iron phase which seems to decrease with increasing laser power. One should stress the excellent agreement between XRD and EDX analysis since not only the decreased Fe peak intensity in the diffractograms cor-



O: γ -Fe₂O₃/Fe₃O₄
x: Fe₃C

FIGURE 2: XRD patterns of samples obtained at three different laser powers: MF10 (70 W), MF04 (50 W), and MF09 (30 W).

responds to the decreasing Fe concentration (see the inset of Figure 1) but also the absolute intensity I_{311} of the Fe_xO_y peak has a decreasing trend, corresponding to the decreasing oxygen concentration given by EDX (see Table 1).

From the results of XRD analysis in Table 2 one may observe that for the as-synthesized iron oxides the a-cell parameter values (identified as either magnetite-Fe₃O₄ (JCPDS 19-0629, a = 0, 8396 nm) or maghemite- γ -Fe₂O₃ (JCPDS 39-1346, a = 0.83515 nm) seem closer to a maghemite phase. The obtained cell parameters for the orthorhombic unit cell of cementite Fe₃C iron carbide were determined using the reflection from the so called “carbide domain” between $2\theta = 37-50^\circ$ (namely (121), (210), (202), (201), (102), (220), (031), (112), (131) carbide reflexions). The as-determined data a = 0.5065 nm, b = 0.6614 nm, and c = 0.4522 nm are in relatively good agreement with the standards ones (a = 0.5091 nm, b = 0.6743 nm, c = 0.4526 nm, JCPDS file 35-0772).

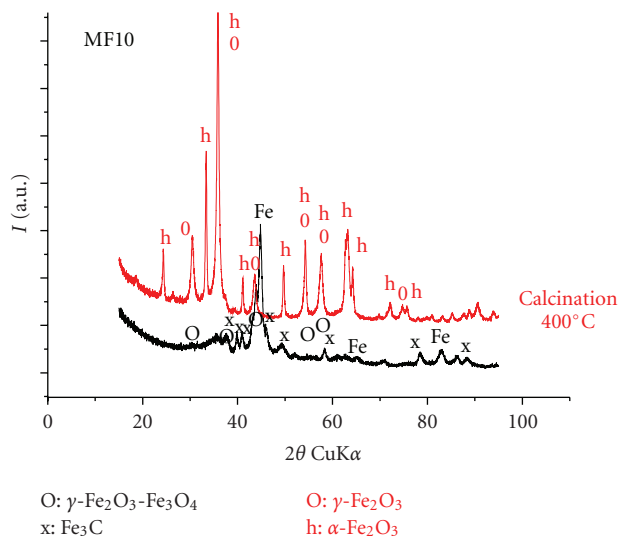


FIGURE 3: XRD patterns for the as-synthesized and the calcined (in air, at 400°C) MF10 sample.

Very small Scherrer crystallite sizes (around 2 nm) in comparison with the other phases were estimated for the spinel-type oxide phase. Much higher dimensions and an increasing trend with laser power seem to characterize the mean crystallite size of the Fe phase (from 9 to about 13 nm in case of MF10 sample). The evaluation of the mean crystallite size for the Fe_3C phase is about 17 nm.

Figure 3 displays a comparison between the diffractograms of the as-synthesized (MF10) and the calcined (MF10h) samples. The thermal treated sample is characterized by increased crystallinity. The XRD pattern of MF10h suggests that this sample is a mixture of the spinel $\gamma\text{-Fe}_2\text{O}_3$ -maghemite phase (JCPDS 39-1346) and the $\alpha\text{-Fe}_2\text{O}_3$ -hematite phase (JCPDS 33-0664). The most probable formation of the maghemite gamma-irons oxide is supported by the parameter value $a = 0.835$ nm (that equals the standard value of 0.83515 nm) and by the presence of additional peaks of low intensity which are absent from the standard magnetite XRD pattern (e.g., in the $2\theta = 23\text{--}27$ region). The maghemite phase appears to have suffered a grain coarsening since the crystallites are sensibly larger, with mean sizes of 12.4 nm as compared to the as-synthesized MF10 (2 nm) (see Table 2). The hematite phase appears as the dominant phase, with well resolved peaks [(012), (104), (214), and (300)] which were used to estimate the cell-parameters ($a = 0.502$ nm and $c = 1.371$ nm) and the average mean crystallite dimension (31.7 nm). It is important to stress that as concerning the mean crystallite dimensions for the calcined MF10h sample, the nanometric character is maintained even if there is an increase in the mean sizes. This observation could be an important attribute in the evaluation of its sensor properties.

3.3. TEM and Particle Distributions. Low-resolution TEM images of the samples MF09, MF04, and MF10 (obtained

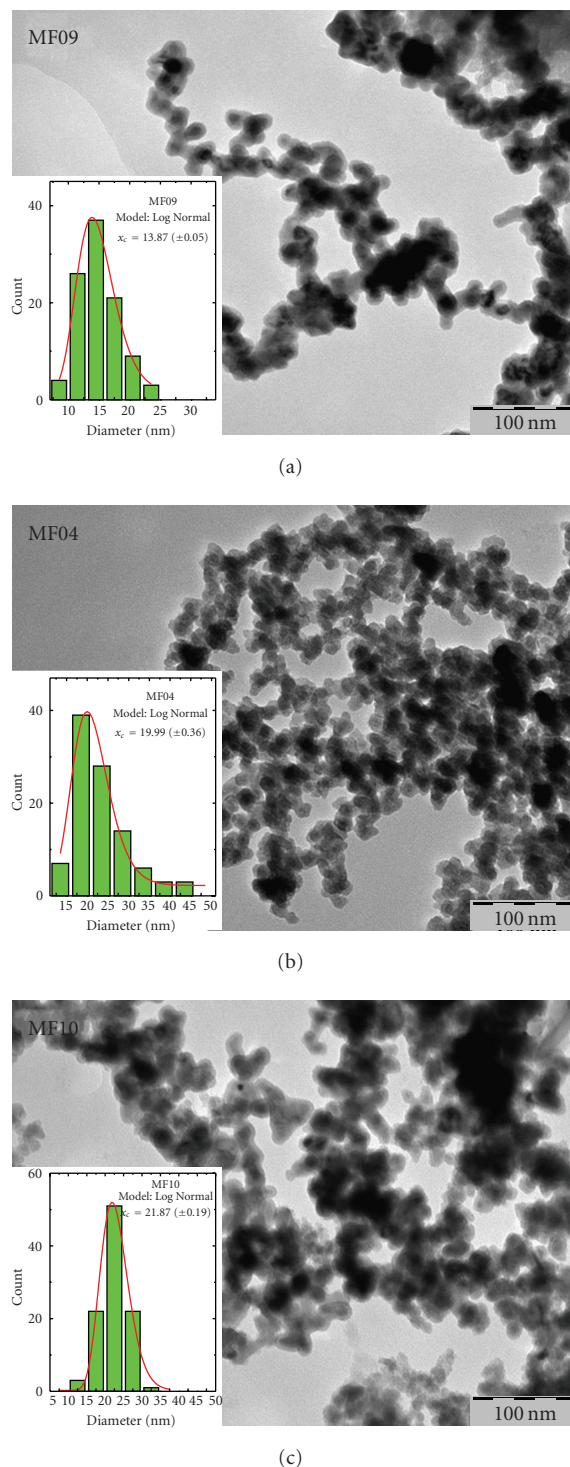


FIGURE 4: Typical low-resolution TEM images of the samples MF09, MF04, and MF10 ((a), (b), and (c), resp.). Their particle diameter distributions are given as insets.

at different laser power densities) are presented in Figures 4(a), 4(b), and 4(c), respectively. The structure of the nanocomposites differing by the content of Fe in them (Table 1) corresponds to agglomerated chains. The sharp

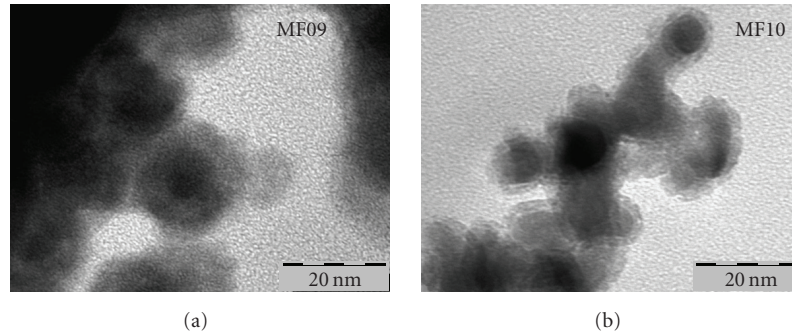


FIGURE 5: Medium resolution TEM images of the nanocomposites: (a) MF09, (b) MF10.

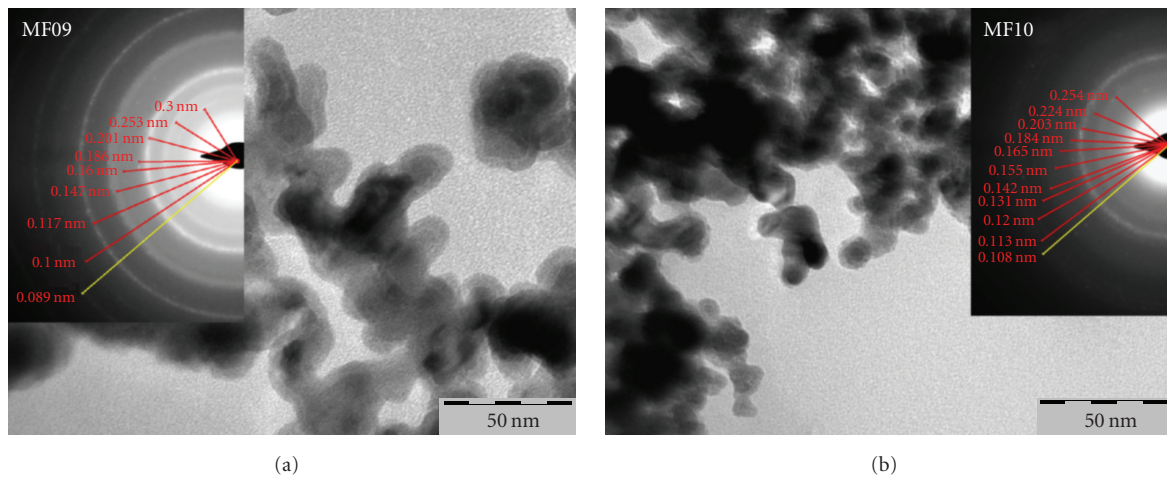


FIGURE 6: The SAED analysis for sample MF09 and MF10.

particle distributions (Log Normal fit) are presented as insets. From the maximum value of the Log Normal fitting function, a rather marked increase of particle diameters with increasing laser power may be noticed, from 14 nm (30 W) to 20 nm (50 W) and 22 nm (70 W).

Medium resolution images of the nanoparticles are presented in Figures 5(a) and 5(b) (samples MF09 and MF10, resp.). Different morphologies seem to characterize these two samples. Thus, the TEM image for the sample obtained at low laser power MF09 reveals nearly spherical balls dark cores encased in a lighter material presumably of polymeric/carbonaceous nature appear. The rather thick coverage presents coalescent features and a “fluffy” appearance. The chain of particles representing sample MF10 (Figure 5(b)) shows frequently the core-shell morphology of round and elongated particles. The shell coverage seems thinner than in sample MF9 and presents apparent discontinuities, suggesting a particulated coverage.

3.4. SAED Structural Analysis. The SAED patterns obtained from a large area of particles, for sample MF09 and MF10 are presented in Figure 6. They exhibit rather diffuse rings (suggesting the formation of amorphous-like or disordered structures). The diffraction rings identification for MF09

points to a major presence of maghemite/magnetite with most intense and broad rings at 0.253 nm [(113) γ Fe_2O_3] and 0.201 nm [(110) α Fe]. The diffraction pattern for sample MF10 suggests overlapping contributions such as the rings at 0.203 nm [Fe_3C -(211), (102), (220), (031), (112) and α Fe (110)] and at 0.165 nm [γ - Fe_2O_3 (333) and Fe_3C (230), (212)].

In the complex laser synthesis process described in this paper, the mechanism of the iron/iron oxide-based nanocomposite formation should consider *the catalytic role of iron nanoparticles*. It is known that, due to its low dissociation energy, the iron pentacarbonyl is the first to dissociate [16]. In the presence of iron nanoparticles formed at high reaction temperature, many competing processes should be considered. Firstly, the catalytic decomposition of MMA monomer at the iron particle surface could lead to the iron-mediated polymerization of MMA. Secondly, the partial degradation of polymerized MMA could lead to carbon fragments. It was found indeed that the thermal degradation of PMMA also leads to the production of char (produced by the elimination of methoxycarbonyl side-chains) [28].

Thirdly, at sufficiently high temperatures, the diffusion of surface carbon into the particle interior is leading to the formation of Fe_3C particles. Accordingly, core-shell

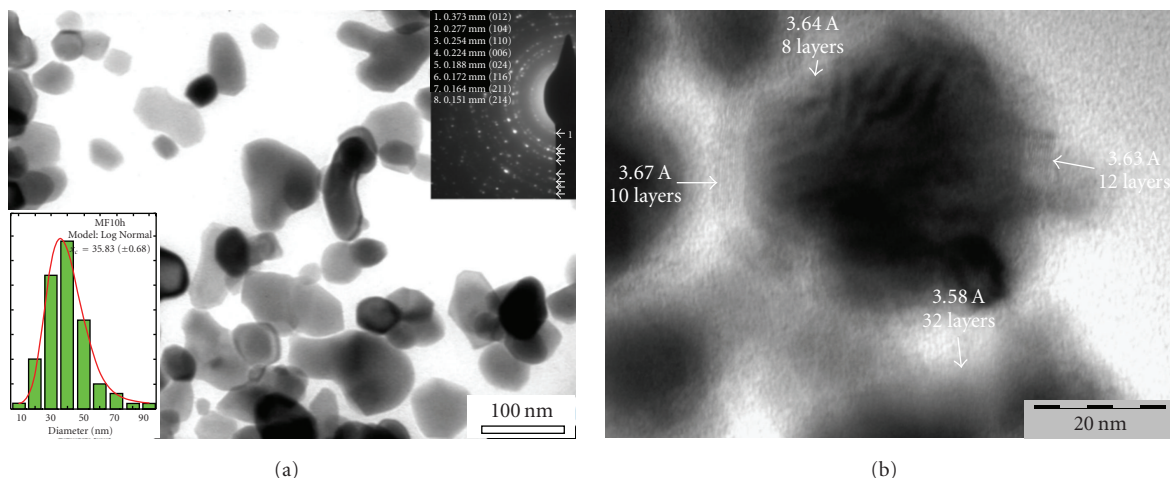


FIGURE 7: (a) Low-resolution TEM images of the sample MF10h (heated in air at 400°C). The left inset present the particle size distribution. SAED analysis is displayed in the right inset. (b) An isolated grain showing layered carbonaceous coverage.

structures are observed which seem to consist of rather crystalline Fe/Fe₃C particles surrounded by shells of variable thickness. At lower laser power, these shells look rather fluffy and should probably consist mostly of polymer. At higher laser power, complementary turbostratic C appears as coverage of nanoparticles (Figure 5(b)).

TEM analysis was also performed on the (heated at 400°C) sample MF10h (Figures 7(a) and 7(b)). Structural changes seem to appear relatively to the as-prepared sample. Irregular particles are observed, many of them still presenting a core shell structure. The darkish outer shell seems now much thinner and more compact than in the as-prepared structures, loosing its “fluffy” character. The diameter distribution of the heated MF10h sample (left inset in Figure 7(a)) is still sharp, pointing a mean value of about 35 nm. In agreement with the XRD, the SAED analysis (right inset in Figure 7(a)) shows increased crystallinity and the coexistence of the α -Fe₂O₃-hematite and Fe₂O₃-maghemite phases. Figure 7(b) presents an isolated grain with layered coverage (variable number of layers, from about 8 to 32) with about 3.6 Å interplanar distance (ascribable to turbostratic carbon). The carbonaceous layers seem to prevail relatively to the possible polymer fragments.

Although the TEM technique used for the analysis of the nanocomposite morphology reveals a complex structure, often consisting of core-shell nanoparticles it does not discriminate the morphologies of the different chemical components of the wrapping layers. Nevertheless, we should underline the importance of the polymeric/carbonaceous shell both for the maintenance of a good dispersion between the small grains and for the protection of freshly formed iron-based cores against the ambient.

3.5. FT-IR Analysis. FT-IR was performed on the nanocomposite Fe/Fe₃O₄-based nanoparticles (IR spectrum of sample MF04 in Figure 8). If we suppose that a partial polymeric shell of the PMMA-type is formed, then we may compare this spectrum with the standard IR spectrum of PMMA in

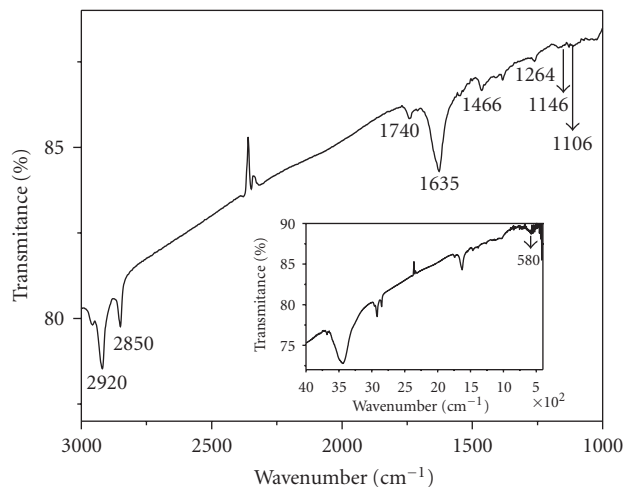


FIGURE 8: The IR spectrum of a representative MF sample (MF04) in the wavenumber region 3000–1000 cm⁻¹. The inset represents the whole IR spectrum (4000–400 cm⁻¹).

which the characteristic IR bands may be assigned according to four main vibration domains: (i) 2850–3050 cm⁻¹ (ascribable to O–CH₃ bond), (ii) 1730 (C=O stretching), (iii) 1685 cm⁻¹ (COO-groups, asymmetric stretch), and (iv) 1140–1180 cm⁻¹ (C–C and C–O cooperative symmetric and asymmetric stretching modes). Some authors [29] attribute to PMMA spectrum also the bands at 1300 and 1450 cm⁻¹ (C–H symmetric and asymmetric stretching modes, resp.). On the MF04 spectrum, these peaks are relatively shifted from the above-mentioned values possibly expressing polymer-metal oxide surface interaction (see also below). The appearance of Fe–C bonds responsible for these IR peak shifts has been supposed [26].

It is worth to mention that in the 2800–3000 cm⁻¹ region, there could be a superposition with the characteristic vibrations of turbostratic/amorphous carbon. Thus, the peaks

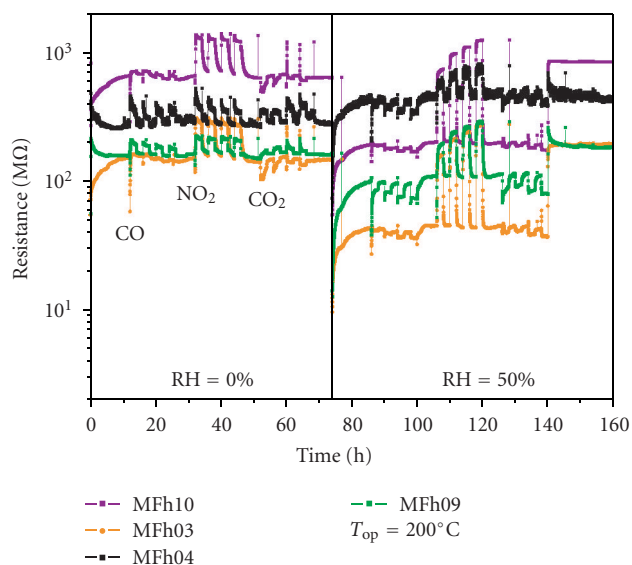


FIGURE 9: The variation of the resistance with CO, NO₂, and CO₂ (different controlled concentrations, see text), in dry atmosphere (0–75 hours time delay) and humid air with RH 50% (75–160 hours time delay), at 200°C working temperature.

appearing at 2820 and 2850 cm⁻¹ are usually ascribed to the C-H stretching vibrations. This observation is consistent with the rather high C content found in the as-synthesized samples (as given by EDX results).

From the whole spectrum presented as inset of Figure 7, one may observe the characteristic bands of iron oxides (usually appearing between 650 and 400 cm⁻¹ with an apparent peak at about 580 cm⁻¹).

It was recently demonstrated by theoretical and experimental work [30] that the interaction of the PMMA segments with the metal (Fe, Al) oxide nanoparticles depends on the regimes of adsorption of polymer chains onto the surfaces (varying curvatures). This interaction induces structural interphase modifications and changes in the infrared spectra of PMMA such as: (i) the decrease in the absorbance of the 2950 cm⁻¹ peak (due to the hydrolysis of methoxy groups); (ii) a relative increase of the 1687 cm⁻¹ peak as compared to the 1734 cm⁻¹ carbonyl peak. Both observations emerge also from our IR analysis in Figure 8.

3.6. The Calcination of Fe/Fe₂O₃-Based Nanocomposites in Relation to Sensor Tests. Referring to the metallic grains of the nanocomposite, the core should undergo step-by-step phase transformation from gamma to alpha oxide phase iron oxide in the temperature range of 300–500°C. The γ -Fe₂O₃ to α -Fe₂O₃ structural transformation may take place at different temperatures depending upon the shell material. Indeed, in [31] it is shown that α -Fe₂O₃ was the only product for the caprylate-capped γ -Fe₂O₃ nanoparticles treated at 400°C, whereas γ -Fe₂O₃ still remained for the γ -Fe₂O₃/PMMA composite treated at 500°C.

If there is rather clear evidence of the transformations suffered by the iron-based core by calcination (around

400°C), the polymer/carbonaceous matrix thermal decomposition seems by far more complex. We suggest that in the present case, polymer total degradation (by a final process of random scission within polymer chains—see below) could be not complete but, partially degraded polymer chains could coexist in the matrix with the carbonaceous fragments (existing also from primary as-synthesized nanocomposite). It is believed [8] that at temperatures lower than 450–500°C, the nanocomposites are more thermally stable than the reference polymer as it may shift upward the degradation temperature of the polymer. On the other hand, it was shown that if T₅₀ is the temperature at which 50% of the original polymeric mass is lost, then the value T₅₀ increased by 30°C for a PMMA composite with metal, synthesized via bulk polymerization [32].

In a study of the thermal stability of PMMA nanocomposites [33] in nitrogen and air, it is found that at temperatures exceeding 150°C, retardation in thermal decomposition for PMMA/silica/titania nanocomposites appears, as compared to PMMA copolymer. In the same reference [33], clear evidence of the existence of three degradation steps for PMMA copolymer are found. The least stable step is attributed to scissions of head-to-head linkages, the second step to scissions at chain-end initiations from vinylidene ends and the third step to random scission within PMMA main chains. The strong interaction between the polymer chains and inorganic particles could prevent PMMA from total thermal decomposition. It is confirmed [34] that the limiting temperature of pyrolysis of pure PMMA copolymer is about 500°C before the deconsolidation rate of the pyrolysis products begins to take control. It was also observed the stabilizing effect of oxygen which may be explained by forming thermally stable radical species that suppress unzipping of the polymer [35].

3.7. Preliminary Sensor Tests. Assuming a semiconducting gas sensor behavior of the Fe/Fe₂O₃-based/nanocomposite, the cross-sensitivity of the thick films was studied by exposing them to nitrogen dioxide, carbon monoxide, carbon dioxide, and different humidity levels. CO and NO₂ toxic gases were chosen due to the utmost importance of their detection since they are toxic at very low concentrations and are frequent in air and exhaust from combustion facilities. CO₂ is generated as a byproduct of the combustion of fossil or vegetable matter (among other chemical processes) being frequently monitored in different applications without considering it as a toxic substance.

For a set of experiments the temperature was maintained constant. One should observe that for “in field” applications, the relative humidity of air cannot be neglected.

Figure 9 shows the variation of the resistance with CO, NO₂, and CO₂ (different controlled concentrations,) for the four MFh samples (MFh10, MFh3, MFh4, and MFh9) (also listed on the figure). The transient characteristics of the electrical resistance for the thick films are displayed in dry atmosphere 0% RH, (0–75 hours time interval, left side of the image) and humid air with RH 50% (75–160 hours time interval, right side of the image). The working

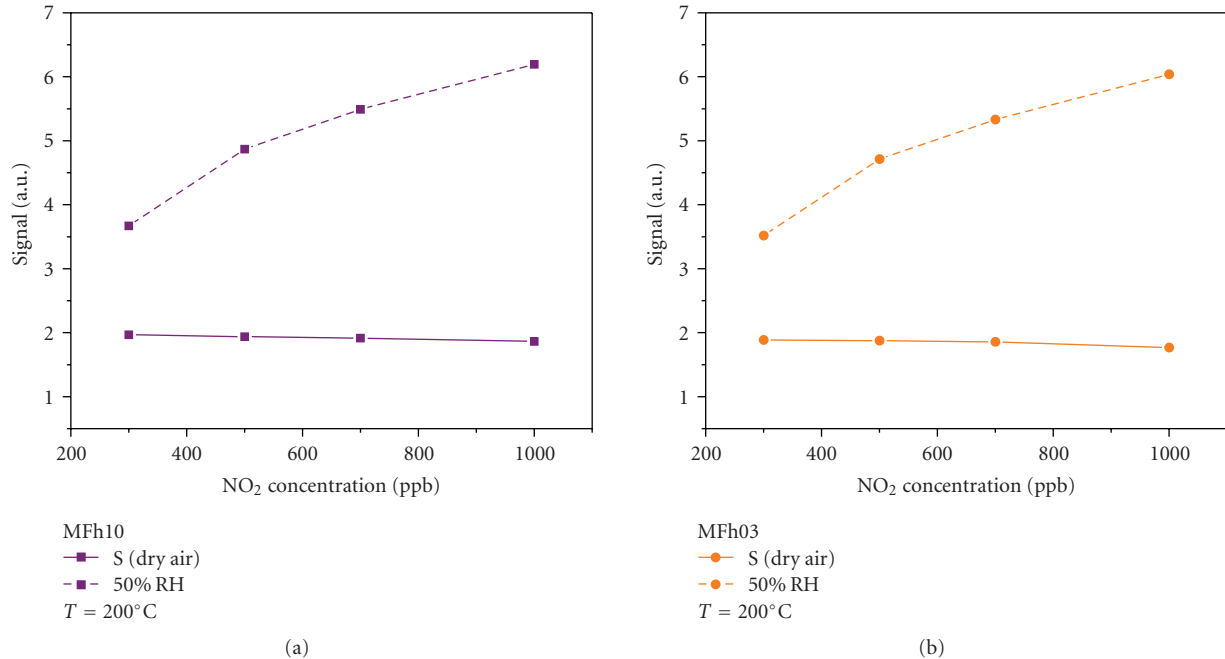


FIGURE 10: The plots of the thick film sensor signals ($\text{Signal} = R_{\text{NO}_2}/R_0$) versus NO_2 concentration, for the MFh10 and MFh03 samples, in dry air and 50% relative humidity, respectively, measured at 200°C temperature.

temperature was maintained at 200°C. The height of the steps corresponds to the concentrations of CO (15, 30, 70, 100 ppm), NO₂ (300, 500, 700, 1000 ppb), and CO₂ (700, 100, 3000, 4000 ppm), respectively. These concentrations were defined in accordance with (time weighted average) TWA international limits. Thus, we set for NO₂ and CO₂ a test concentration range below the TWA limits and a spread concentration range for CO gas (e.g., OSHA limits: NO₂-5ppm; CO₂-5000 ppm; CO-30 ppm).

One may observe that in humid air atmosphere (50% RH) which is similar to the usual in field atmospheres, a pronounced increased of the film resistance towards NO₂ exposure (*p*-type conduction) and a slightly decrease in the presence of CO and CO₂ gases (*n*-type conduction). An *n*-to-*p*-type conductivity transition induced by oxygen adsorption on $\alpha\text{-Fe}_2\text{O}_3$ was already reported [36]. The relative humidity has a strong effect on the CO response [37] since it is related to the surface reactions between CO and the chemisorbed oxygen. The coadsorbed water may change states and reactivities of the adsorbed oxygen and consequently, the sensor response.

It was also suggested that *n*- or *p*-type conduction is observed due to the low formation enthalpy of intrinsic defects, such as oxygen vacancies [38].

It is worth to note that, from the point of view of NO₂ detection, both MFh10 and MFh03 samples will be further analyzed because they exhibit (i) higher sensitivity than the other two samples (MFh04 and MFh09) and (ii) NO₂ selectivity [39] relatively to CO and CO₂. Much more, remarkable stable and reproducible sensor response may be noticed (see also below). In Figure 10, the variation of the sensor signal in NO₂, for samples MFh10 and

MFh03, respectively, is presented. The sensor signal *S* is defined as the ratio R_{NO_2}/R_0 where R_{NO_2} and R_0 are the resistance values measured in presence and in absence of NO₂ concentrations. For both samples, the signal is recorded in dry air (lower curves) and 50% relative humidity (upper curves). Rather high sensitivity for the MFh10 nanomaterial may be observed, $S = 5.7$ for 800 ppb NO₂ in humid air, at an operating temperature of 200°C. Here again the catalytic role of water vapors may be suggested.

The dependence of the sensor signal on the working temperature is an expression of the temperature dependence of the interaction between the sensor active surface layers and the surrounding gases which depends on the dissociation energies, the adsorption, the chemical reactions, the desorption, and so forth. As mentioned before, the sensor tests for all samples MFh have been carried out at different working temperatures. Figure 11 displays the variation of the resistance at a higher working temperature ($T = 250^\circ\text{C}$). A decrease of the sensor signal is noticeable, probably due to the increased desorption rate. On the other hand, at temperatures lower than 200°C the signal becomes less stable and poorly reproducible and the reference resistance increases by an order of magnitude. Thus our results suggest the existence of an optimum 200°C temperature for the detection of NO₂ in humid air. This fact corroborated with the evidence of the rather high sensitivity to NO₂ of the MFh10 sample could recommend this nanomaterial in applications for NO₂ toxic gas detection.

It is worth to note that preliminary experiments show that, besides sensitivity and selectivity, these materials seem to present also very good response and recovery times (after the exposure to the different NO₂ gas concentrations or/and

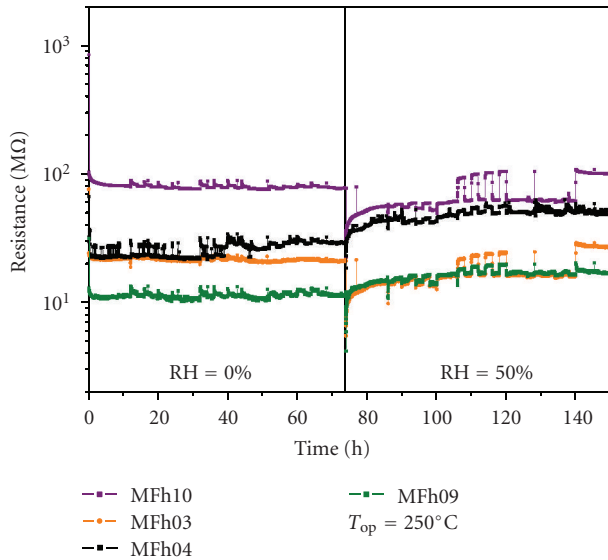


FIGURE 11: The variation of the resistance with CO, NO₂, and CO₂ (different controlled concentrations), in dry atmosphere (0–75 hours time delay) and humid air with RH 50% (75–160 hours time delay) (250°C working temperature).

to humidity). Much more, a good stability for sample MF10 is suggested by performing experiments (not presented here) in which the resistance recovers the initial value R_0 (about 200 MΩ without test gases) after the different exposures to NO₂ (after the stimuli have ceased). We should mention however that at this stage, the goal of our investigations was merely phenomenological, intending to study the cross-sensitivity of the sensing structures. A thorough analysis of the other sensor parameters, most important for practical applications (such as the response and the recovery time, the sensor calibration curve and its temporal stability, etc.) is the concern of currently developing investigations.

As described before, the Fe/Fe₂O₃-based/nanocomposite possess a dominant core-shell structure which could manifest a sensing behavior primary due to the iron oxide-based core. In this connection, the better material stability offered by the hematite relatively to other iron oxide phases such as maghemite should be considered. A nanometric structure presenting a high-surface area will enhance the sensing properties. Indeed, the processing of the sensing material ensures a grain size in the nanometric range, even after air calcination (see Figure 7). However, for explaining the observed sensitivity one should take into account not only the Fe₂O₃ content but also the polymeric/carbonaceous matrix: (i) the particle coating maintains a good dispersion between the small grains (coatings prevents grain growth and agglomeration) thus avoiding sintering; (ii) the carbonaceous shell could act like a stabilizer for the oxide phase at higher temperatures; (iii) the appearance of nanometric-size channels, due to the loss of gas and shrinkage in volume could favor gas penetration onto the Fe₂O₃ interface [40]; (iv) the probably low contribution of the carbonaceous component of the calcined composite to the semiconductivity of the thick film should not be neglected. In fact it is already

known that, depending on the chemical process and on the heating temperature, amorphous carbon could present different degrees of semiconductivity [41].

The different sensitivities towards the test gases presented by the samples MF could appear due to their different chemical composition, their nanostructures, the crystallite dimensions, and the nature of defects.

The adsorption of species like O₂⁻, O⁻, O²⁻, OH⁻ which may capture electrons from the conduction band determines a negative charge of the surface. Consequently, close to the surface, due to repulsive forces a diminished concentration of free electrons will appear. For samples with high developed specific surfaces this will result in a lowered conductance, that is, an increase of the electrical resistance. This experimental behavior of the electrical resistance is characteristic for synthetic air and oxidizing gases (NO₂).

The applicative demands (particularly in the automotive industry) concerning the detection of the presence of NO₂ as a very harmful gas are higher than those asking for the precise measurement of the existing NO₂ concentration. Consequently, at this early stage of the research, sample MF10h may be considered as a promising nanomaterial for this kind of applications.

4. Conclusions

Iron/iron oxide-based nanocomposites were prepared by IR laser-induced and C₂H₄-photosensitized codecomposition of Fe(CO)₅ and MMA. Mainly core-shell structures were observed. Different analytical techniques evidence the cores as formed mainly by iron/iron oxide crystalline phases. A partially degraded (carbonized) polymeric matrix is supposed for the coverage of the metallic particles. The nanocomposite structure at the variation of the laser density and of the MMA monomer flow was studied. The potential of the new material for acting as gas sensor was tested on the material prepared as thick films. The variation of the electrical resistance in presence of NO₂, CO, and CO₂, in dry and humid air was recorded. Preliminary results show that the samples obtained at higher laser power density exhibit rather high sensitivity towards NO₂ detection and NO₂ selectivity relatively to CO and CO₂. An optimum working temperature of 200°C was found. Further studies will focus on the different factors influencing the sensor response and the stability.

Acknowledgments

The authors gratefully acknowledge the partial financial support from the Romanian Ministry of Education and Research through the Projects PNCD II PARTENERIATE (71/083/2007) and PNCD II IDEI (431/2007).

References

- [1] J. Jordan, K. I. Jacob, R. Tannenbaum, M. A. Sharaf, and I. Jasiuk, "Experimental trends in polymer nanocomposites—a review," *Materials Science and Engineering A*, vol. 393, no. 1-2, pp. 1–11, 2005.

- [2] L. F. Nicolais and G. Carotenuto, "Synthesis of polymer-embedded metal, semimetal, or sulfide clusters by thermolysis of mercaptide molecules dissolved in polymers," *Recent Patents on Materials Science*, vol. 1, pp. 1–11, 2008.
- [3] S. Rifai, C. A. Breen, D. J. Solis, and T. M. Swager, "Facile in situ silver nanoparticle formation in insulating porous polymer matrices," *Chemistry of Materials*, vol. 18, no. 1, pp. 21–25, 2006.
- [4] F. Hussain, M. Hojjati, M. Okamoto, and R. E. Gorga, "Polymer-matrix nanocomposites, processing, manufacturing, and application: an overview," *Journal of Composite Materials*, vol. 40, no. 17, pp. 1511–1575, 2006.
- [5] C. Sanchez, B. Julian, Ph. Belleville, and M. Popall, "Applications of hybrid organic-inorganic nanocomposites," *Journal of Materials Chemistry*, vol. 15, no. 35–36, pp. 3559–3592, 2005.
- [6] S. C. K. Misra, P. Mathur, and B. K. Srivastava, "Vacuum-deposited nanocrystalline polyaniline thin film sensors for detection of carbon monoxide," *Sensors and Actuators A*, vol. 114, no. 1, pp. 30–35, 2004.
- [7] Z. Jia, Z. Wang, C. Xu, et al., "Study on poly(methyl methacrylate)/carbon nanotube composites," *Materials Science and Engineering A*, vol. 271, no. 1–2, pp. 395–400, 1999.
- [8] C. Aymonier, D. Bortzmeyer, R. Thomann, and R. Lhaupt, "Poly(methyl methacrylate)/palladium nanocomposites: synthesis and characterization of the morphological, thermomechanical, and thermal properties," *Chemistry of Materials*, vol. 15, no. 25, pp. 4874–4878, 2003.
- [9] Z. Guo, L. L. Henry, V. Palshin, and E. J. Podlaha, "Synthesis of poly(methyl methacrylate) stabilized colloidal zero-valence metallic nanoparticles," *Journal of Materials Chemistry*, vol. 16, no. 18, pp. 1772–1777, 2006.
- [10] X. Gou, G. Wang, J. Park, H. Liu, and J. Yang, "Monodisperse hematite porous nanospheres: synthesis, characterization, and applications for gas sensors," *Nanotechnology*, vol. 19, no. 12, Article ID 125606, 7 pages, 2008.
- [11] S. Si, Ch. Li, X. Wang, Q. Peng, and Y. Li, "Fe₂O₃/ZnO core-shell nanorods for gas sensors," *Sensors and Actuators B*, vol. 119, no. 1, pp. 52–56, 2006.
- [12] D. N. Suryawanshi, D. R. Patil, and L. A. Patil, "Fe₂O₃-activated Cr₂O₃ thick films as temperature dependent gas sensors," *Sensors and Actuators B*, vol. 134, no. 2, pp. 579–584, 2008.
- [13] D. Meka, V. Onbattuvelli, S. Atre, and S. Prasad, "Palladium/polymer nanocomposite based chemiresistive SO₂ sensor," in *Clean Technology*, vol. 4, pp. 412–415, 2008.
- [14] K. Arshak, E. Moore, C. Cunneffe, M. Nicholson, and A. Arshak, "Preparation and characterisation of ZnFe₂O₄/ZnO polymer nanocomposite sensors for the detection of alcohol vapours," *Superlattices and Microstructures*, vol. 42, no. 1–6, pp. 479–488, 2007.
- [15] A. Galykova, Z. Bastl, R. Alexandrescu, I. Morjan, and J. Pola, "Thermal behaviour of polyoxocarbo-silane shells in Fe-based (core)-polyoxocarbo-silane (shell) nanocomposites," *Thermochimica Acta*, vol. 439, no. 1–2, pp. 80–85, 2005.
- [16] R. Alexandrescu, I. Morjan, I. Voicu, et al., "Combining resonant/non-resonant processes: nanometer-scale iron-based material preparation via CO₂ laser pyrolysis," *Applied Surface Science*, vol. 248, no. 1–4, pp. 138–146, 2005.
- [17] A. Tomescu, R. Alexandrescu, I. Morjan, et al., "Structural and sensing properties of a novel Fe/Fe₂O₃/polyoxocarbo-silane core shell nanocomposite powder prepared by laser pyrolysis," *Journal of Materials Science*, vol. 42, no. 5, pp. 1838–1846, 2007.
- [18] R. Roescu, I. Dumitriu, and A. Tomescu, "Simultaneous evaluation of the electrical resistance and work function changes for chemoresistive type sensors," *Romanian Reports in Physics*, vol. 56, no. 4, pp. 607–612, 2004.
- [19] J. Pola, "Laser powered homogeneous decomposition of methyl acrylate and methacrylate," *Tetrahedron*, vol. 45, no. 16, pp. 5065–5072, 1989.
- [20] A. Gandini, "The interaction of pulsed CO₂-laser radiation with common monomers," *Canadian Journal of Chemistry*, vol. 55, pp. 4045–4047, 1977.
- [21] B. Zhang and F. D. Blum, "Thermogravimetric study of ultrathin PMMA films on silica: effect of tacticity," *Thermochimica Acta*, vol. 396, no. 1–2, pp. 211–217, 2003.
- [22] P. Nising, T. Meyer, R. Carloff, and M. Wicker, "Thermal initiation of MMA in high temperature radical polymerizations," *Macromolecular Materials and Engineering*, vol. 290, no. 4, pp. 311–318, 2005.
- [23] M. Jose, A. Sales, and G. G. de Barros, "Effect of iron(III) oxide on the thermal polymerization of methyl methacrylate in low density polyethylene matrix," *Polymer Bulletin*, vol. 36, no. 4, pp. 495–502, 1996.
- [24] P. Zhi-Da, S. Jun-Quan, and Y. Shi-Lin, "Polymerization of methyl methacrylate with iron-ytterbium dinuclear metal-ocene catalyst," *Journal of Zhejiang University A*, vol. 1, pp. 20–26, 2000.
- [25] L. Ravikumar and R. Thevi, "Polymerization of methyl methacrylate by ziegler-natta type catalyst systems: Fe(acac)₃-AlEt₂Br and Fe(acac)₃-ZnEt₂Br," *Polymer Science, Series B*, vol. 50, no. 9–10, pp. 227–231, 2008.
- [26] D. R. S. Somayajulu, C. N. Murthy, D. K. Awasthi, N. V. Patel, and M. Sakkar, "Mössbauer studies of iron doped poly(methyl methacrylate) before and after ion beam modification," *Bulletin of Materials Science*, vol. 24, no. 4, pp. 397–400, 2001.
- [27] I. Morjan, R. Alexandrescu, M. Scarisoreanu, et al., "Controlled manufacturing of nanoparticles by the laser pyrolysis: application to cementite iron carbide," *Applied Surface Science*, vol. 255, no. 24, pp. 9638–9642, 2009.
- [28] T. Caykara, M. S. Eroglu, and O. Guven, "Thermal and oxidative degradation of vinyl triethoxy silane-methyl methacrylate copolymers," *Polymer Degradation and Stability*, vol. 63, no. 1, pp. 65–70, 1999.
- [29] S. Ahmad, S. Ahmad, and S. A. Agnihotry, "Synthesis and characterization of in situ prepared poly (methyl methacrylate) nanocomposites," *Bulletin of Materials Science*, vol. 30, no. 1, pp. 31–35, 2007.
- [30] E. Hershkovits, A. Tannenbaum, and R. Tannenbaum, "Polymer adsorption on curved surfaces: a geometric approach," *Journal of Physical Chemistry C*, vol. 111, no. 33, pp. 12369–12375, 2007.
- [31] T. Ninjbadgar, S. Yamamoto, and M. Takano, "Thermal properties of the γ -Fe₂O₃/poly(methyl methacrylate) core/shell nanoparticles," *Solid State Sciences*, vol. 7, no. 1, pp. 33–36, 2005.
- [32] E. Kandare, H. Deng, D. Wang, and J. M. Hossenlopp, "Thermal stability and degradation kinetics of poly(methyl methacrylate)/layered copper hydroxy methacrylate composites," *Polymers for Advanced Technologies*, vol. 17, no. 4, pp. 312–319, 2006.
- [33] H. Wang, P. Xu, S. Meng, W. Zhong, W. Du, and Q. Du, "Poly(methyl methacrylate)/silica/titania ternary nanocomposites with greatly improved thermal and ultraviolet-shielding properties," *Polymer Degradation and Stability*, vol. 91, no. 7, pp. 1455–1461, 2006.

- [34] H. Arisawa and T. B. Brill, "Kinetics and mechanisms of flash pyrolysis of poly(methyl methacrylate) (PMMA)," *Combustion and Flame*, vol. 109, no. 3, pp. 415–426, 1997.
- [35] J. D. Peterson, S. Vyazovkin, and C. A. Wight, "Kinetic study of stabilizing effect of oxygen on thermal degradation of poly(methyl methacrylate)," *Journal of Physical Chemistry B*, vol. 103, no. 38, pp. 8087–8092, 1999.
- [36] T. Sahm, L. Mädler, A. Gurlo, N. Barsan, S. E. Pratsinis, and U. Weimar, "Flame spray synthesis of tin dioxide nanoparticles for gas sensing," *Sensors and Actuators B*, vol. 98, no. 2-3, pp. 148–153, 2004.
- [37] G. Neri, A. Bonavita, S. Galvagno, P. Siciliano, and S. Capone, "CO and NO₂ sensing properties of doped-Fe₂O₃ thin films prepared by LPD," *Sensors and Actuators B*, vol. 82, no. 1, pp. 40–47, 2002.
- [38] R. Van de Krol and H. L. Tuller, "Electroceramics—the role of interfaces," *Solid State Ionics*, vol. 150, no. 1-2, pp. 167–179, 2002.
- [39] S. Brahim-Belhouari, A. Bermak, M. Shi, and P. C. H. Chan, "Fast and robust gas identification system using an integrated gas sensor technology and Gaussian mixture models," *IEEE Sensors Journal*, vol. 5, no. 6, pp. 1433–1444, 2005.
- [40] O. K. Varghese and C. A. Grimes, "Metal oxide nanoarchitectures for environmental sensing," *Journal of Nanoscience and Nanotechnology*, vol. 3, no. 4, pp. 277–293, 2003.
- [41] H. Kuroda and E. A. Flood, "Effect of ambient oxygen on the semiconductivities of evaporated films of mesonaphthodanthrene and mesonaphthodianthrone," *Canadian Journal of Chemistry*, vol. 39, pp. 1475–1483, 1961.



Hindawi

Submit your manuscripts at
<http://www.hindawi.com>

